Data Science Approaches for Tracking Electrochemical Reactions and Phase Transformations

Chih-Wei Hsu

A thesis

submitted in partial fulfillment of the

requirements for the degree of

Master of Science in Chemical Engineering

University of Washington

2020

Reading Committee:

Vincent C. Holmberg, Chair

David A. C. Beck

Program Authorized to Offer Degree:

Chemical Engineering

University of Washington

Abstract

Data Science Approaches for Tracking Electrochemical Reactions and Phase Transformations

Chih-Wei Hsu

Chair of the Supervisory Committee:
Assistant Professor Vincent C. Holmberg
Department of Chemical Engineering

Battery characterization techniques give critical information about what is happening inside the battery. However, fully utilizing the data obtain via battery characterization, particularly battery cycling can be difficult, because so many data points are produced during battery cycling. A more recent innovation in battery characterization is to leverage data science to more fully utilize information obtained during various battery cycling protocols. Herein, we introduce two examples of using data science approaches[1–5] combined with the battery characterization to maximize the value of the characterization data: total differential capacity (dQ/dV) plots[6–10] and galvanostatic intermittent titration technique (GITT).[11]

Total differential capacity plots are a powerful tool for understanding battery degradation when combined with various characterization techniques. However, due to the large amount of

data, it is difficult to obtain quantitative conclusions via visual analysis, the typical approach for total differential capacity analysis. As a result, a data science approach[8] was proposed to support quantitative conclusions for total differential capacity analysis. Herein, a software package[8] has been developed to quantitatively analyze the battery cycling data from the dQ/dV plots. In addition, a user interface was built up and some documentations and demonstrations were set up to help the users have a better understanding of the codes and make it more accessible to use.

Besides the application in tracking the electrochemical reactions within the battery, data science can also be combined with GITT to extract[12–20] thermodynamic and kinetic data from a battery. This work focuses on generalizing a previously developed novel GITT model[14] that accurately determined the lithium ion diffusions coefficient for a two-phase[21,22] lithium iron phosphate electrode, so that the model can readily be applied to any phase transformation battery electrode ($LiFePO_4$) system.[21–25] We validate our generalized tool both by replicating the data from the previous work[14] and using the generalized tool to determine the sodium ions diffusion coefficients in the two-phase region during the sodium antimonide (Na_3Sb)[26–30] battery charge-discharge cycling. In the standard GITT diffusivity model[14,18], the diffusion coefficients can appear to be many of magnitude lower in the two-phase region. This apparent drop occurs because phase-transformation is not considered in the GITT diffusivity model. Therefore, the novel phase-transformation GITT diffusivity model[14] that we develop into a tool in this work takes both the diffusion and the interface migration[23] into account. By solving the 1-D diffusion partial differential equations (PDEs)[31–33] with the corresponding moving boundary conditions, the concentration profile, and the diffusion coefficients in both α and β phase can be determined. The diffusion coefficients obtained by the new model in the two-phase region are about

$10^{-15} \sim 10^{-14}\ cm^2/s$ for α and β phase, which is validated by the similarity of the diffusion coefficients calculated by the standard model[14,18] in the single-phase region.

TABLE OF CONTENTS

LIST OF FIGURES

LIST OF TABLES

ACKNOWLEDGEMENTS

This thesis might not exist without the support of many brilliant, encouraging, and passionate people in my life. First and foremost, I would like to thank my advisor, Dr. Vincent Holmberg for having been constantly supportive and encouraging over the past few years. Thank you that the door of your office is always open for guidance and encouragements both in my research and career planning. Your support and encouragement of creativity and inspiration helped me grow as a researcher, and an engineer. I am also thankful to other committee member, Professor David Beck, for providing valuable and supportive feedback toward my work.

I am extremely grateful to my group members for your help and support in these two years. I want to thank Nicole Thompson for guiding me when I just started to learn programming Python and illustrating many data science concepts for me. Thanks to Grant Williamson for always answering my electrochemical questions and providing beneficial suggestions in both my research and thesis writing. Thanks to Soohyung Lee for guiding and training me in the nanoparticles synthesis through the Schlenk Line process. I am also extremely appreciative of Elena Pandres and Brittany Bishop, thank you for helping me in my thesis preparation, all your feedback and suggestions have been indispensable to my thesis writing. Thank you to current and former lab mates, including, Guesang Kevin Lee, Ge Gu, Yao-Yu Li, for scientific and moral support.

I also want to thank my friends for inspiring and supporting me during my time at UW. In particular, I want to thank Kun-Lin Wu, Shao-Fung Hsu, Gouyao Chen, Kailei Liu, Zizhao Xu, Zonglun Li, Sijin Luozhong, and Kuanhsun Liu. Thank you all for constantly being part of my life

when studying abroad in Seattle and making here feel more like home. I am also incredibly appreciative of Melody Cheng for being a constant source of encouragement and enthusiasm over the years, thank you for being an exceptional partner in and out of the pursuit of my Masters.

I also feel blessed to meet all the saints in Seattle, thank you for your encouraging words and both spiritual and practical support during my time here. In particular, I want to give thanks to current and former brothers living in the brothers' house, including Tianyi Ma, Vincent Pau, Sylas Sun, Jeremy Schoenfeld, Paul Berdnikov, Steven Yen, Minsu Gim, Ken Latimer, James Little, Jui-Yun Chang, Timothy Kwan, Mathew Teng, Timothy Bi, Hang Guo, Kibum Kim, Ian Bae, Melchisedec Lai, Jiahao Han, David Hsu, Peter Zheng, Timothy Chen, Billy Tao and Weilung Ho. Thank you guys for making this house so sweet and warm. I also want to give special thanks to the Peng's, thank you for the support and shepherding over the past few years, it is so blessed that I could meet you when I just arrived a new environment, and not too many people share the same culture with me.

Finally, I am indebted to my family, who is always supporting and encouraging me to pursue my dream. Thank you, my dear parents, thank you for all your hard work to support my education and living in Seattle. Without your support, it is impossible for me to have the achievement I have today.

Chapter 1. INTRODUCTION

1.1 Data Science Approaches for Evaluating Battery Performance

1.1.1 *The Role of Data Science in Battery Characterization*

A wide range of battery characterization techniques are critical for developing a strong understanding[34–36] of degradation processes in order to design materials and architectures to improve the lifetime, capacity, and rate capability. Battery cycling experiments typically produce large amounts of data. The resulting battery data is frequently analyzed through qualitative methods, often omitting a significant amount of data and cycles, which can result in an incomplete picture of battery performance. The existing battery cycling data can be mined further to develop a better understanding of battery performance and degradation mechanisms. Data science[1–5] offers an ideal approach for supporting rapid quantitative analysis of various battery systems. This thesis will cover the development of several data science approaches[8] for the battery characterization in order to develop a more detailed and quantitative picture of battery materials characterization.

1.1.2 *A Common Technique for Battery Characterization: Total Differential Capacity Plots Analysis*

As anyone with a smart phone knows, battery performance degrades over time. When you first get the phone, you might have 8 hours of battery life after a single charge, but after a year, the lifetime may decrease to 2 or 3 hours. One of the clearest pictures of battery degradation is the capacity vs. cycle number plot, which is shown in Figure 1.1. This is plot shows how capacity fades over iterative cycling, but it omits many of the details that can be helpful in identifying degradation mechanisms.

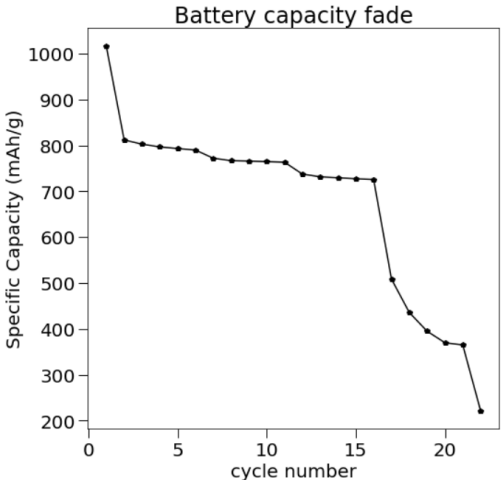

Figure 1.1 An example of the battery capacity fade over cycles.

Therefore, the potential vs. specific capacity plot, which is shown in Figure 1.2, allows us to observe multiple cycles of charge and discharge cycles at the same time, and it also helps us understand how the capacity changes with different slopes as the potential changes. The difference both in charge and discharge between the 5th and the 25th cycle are shown in Figure 1.2.

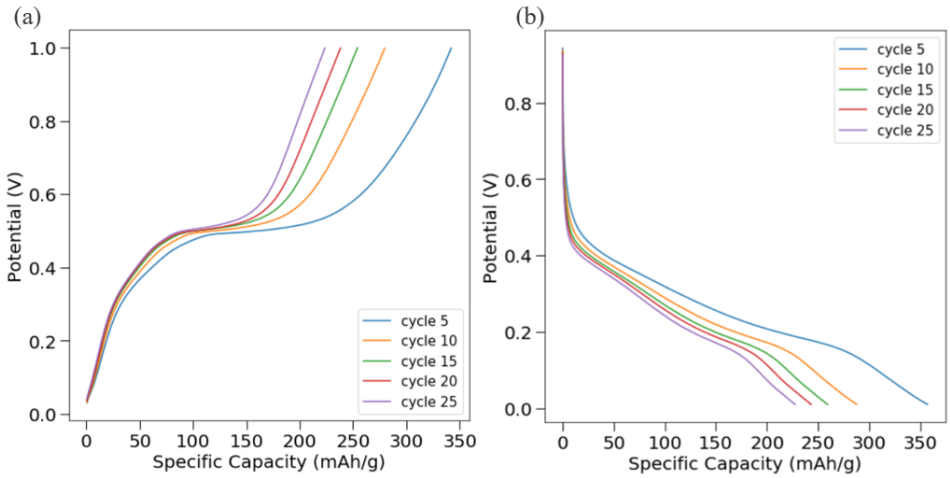

Figure 1.2. An example for the potential vs. specific capacity plot of (a) charge cycle, and (b) discharge cycle.

However, in order to advance battery performance, we need to develop a more detailed picture to pinpoint how and when batteries lose capacity. Ideally, we would like to visualize and

understand how each electrochemical event changes during every cycle; however, showing the potential vs. capacity curve for each cycle would make it visually difficult to identify important changes that are associated with capacity fade. On the other hand, performing a qualitative analysis on a figure that only shows a subset of the battery cycles makes it difficult to extract important features associated with capacity fade during electrochemical cycling that are not displayed. With the huge amount of data produced during battery cycling, subtle changes over the cycles are difficult for human eyes to observe. In other words, it is not immediately intuitive where the capacity fade mechanism happens.

To enhance the subtle changes that are difficult to identify through qualitative analysis by the human eye, many researchers use total differential capacity plot analysis to further understand why the performance of battery materials change throughout cycling. In the plot of the derivative of a battery's capacity versus voltage, the flat plateaus during charging and discharging turn into peaks as shown in Figure 1.3b below, as known as a total differential capacity (dQ/dV) plot. As a result, the changes in the dQ/dV plot are easier for human eyes to observe, and the changes throughout cycling are more apparent as we look at multiple cycles. Total differential capacity analysis highlights how the various electrochemical events[9] in the battery evolve over iterative cycling. When combined with various characterization techniques such as *in situ* X-ray diffraction (XRD)[37], nuclear magnetic resonance (NMR) spectroscopy[38], Raman[39], or Synchrotron scattering[40], total differential capacity analysis is a powerful tool for understanding battery degradation process.

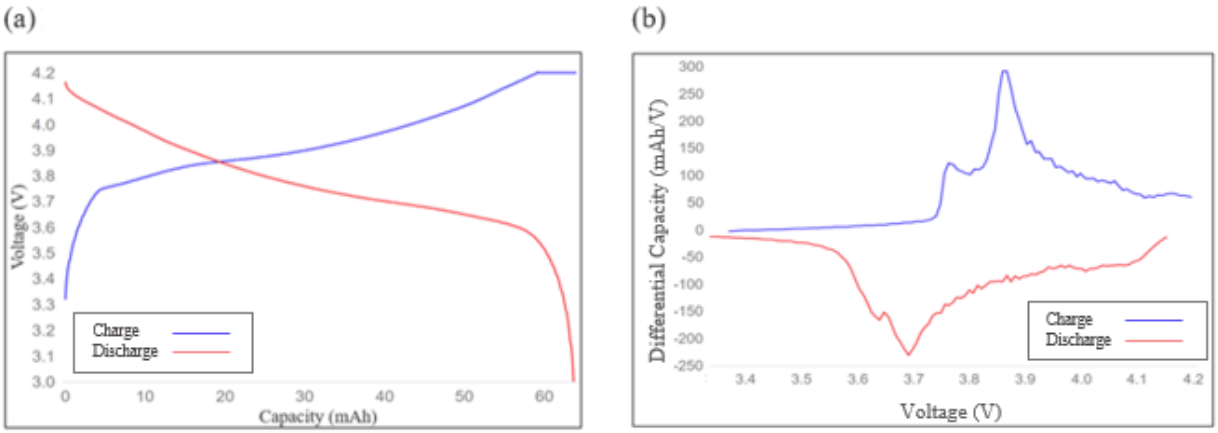

Figure 1.3. An example for a (a) capacity vs. potential plot and a (b) total differential capacity (dQ/dV) plot. For both plots, the charge cycle is in blue and the discharge cycle is in red.

1.1.3 *Leveraging Data Science to Improve the Evaluation of Battery Performance*

Although a qualitative analysis of total differential capacity plots provides more insight into battery performance, the large amount of data—often hundreds of thousands of datapoints—makes it difficult to obtain quantitative analysis and conclusions. For example, it is clear that the peaks in the dQ/dV plot in Figure 1.4 shift or change in intensity throughout cycling, indicated by the red arrows; however, without knowing the accurate location of each peak, it is difficult to determine how much the peaks shift or decrease as cycling continues. These quantitative values would provide important information related to how the change in the charge passing through each reaction as well as increased or decreased resistance as the battery ages.

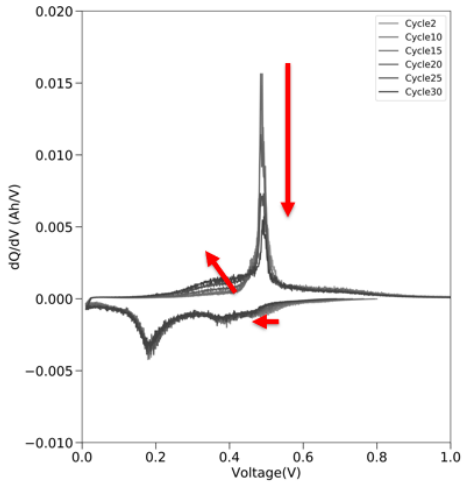

Figure 1.4. A total differential capacity plot, with arrows demonstrative qualitative shifts in voltage and intensity of peaks in the total differential capacity plot.

To address this problem, we have developed a series of data science approaches[8] to support the analysis of differential capacity plots to label each peak as well as track the change in voltage and intensity of each peak. First, data cleaning was applied to eliminate noise in the background of the data and make the dQ/dV curve smoother[7]. Second, a peak fitting model[41] was used to identify the voltage position information of each peak. Finally, that information of the peaks was shown as the descriptors and visualized on a plot for the users. Herein, the data science approach which mentioned above will be illustrated in detail from the Python package requirements to visualization the results. My individual work in this section focused on developing the documentations of these packages and the demonstration of their utility to ensure these analysis techniques could be used by future researchers as a tool that could be readily applied to new systems.

1.2 GITT Method for Determining Diffusion Coefficients during Phase Transformation

1.2.1 *Galvanostatic Intermittent Titration Technique (GITT)*

The galvanostatic intermittent titration technique (GITT)[11] is a common procedure to retrieve both thermodynamic and kinetic parameters from battery materials, which helps develop a better understanding of the electrochemical behavior of the battery. In the procedure of GITT, as shown in Figure 1.5 and 1.6, a series of current pulses are applied to the battery, and after each current pulse a relaxation period, a period in which no current passes through the cell, is applied to the battery.

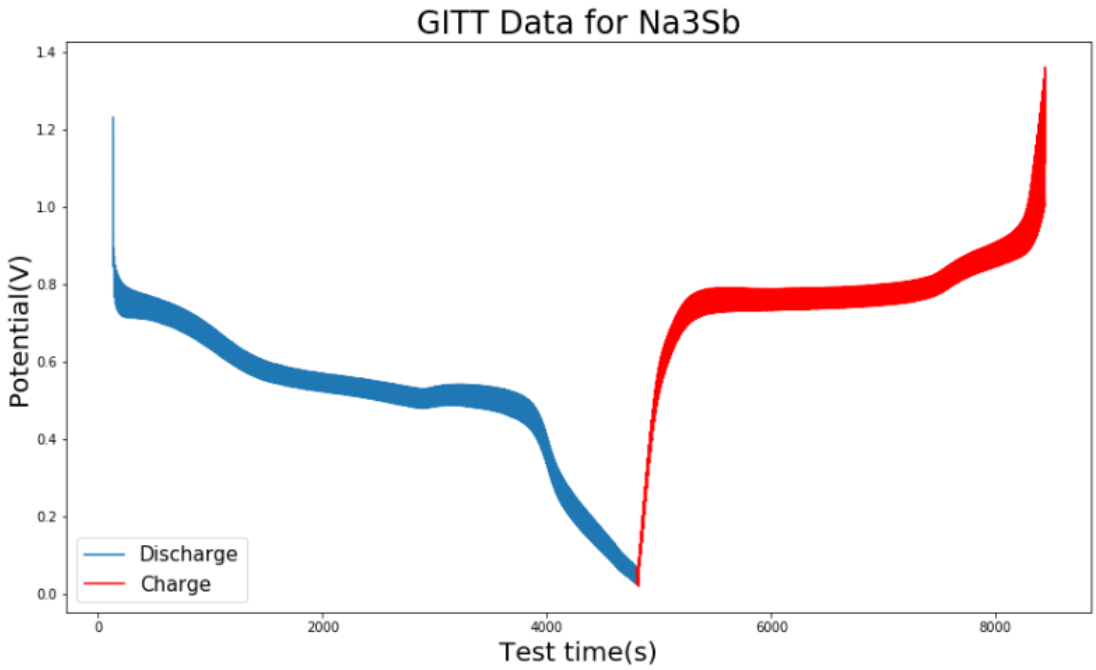

Figure 1.5. Example of the GITT curves of Na_3Sb, discharge cycle is in blue and the charge cycle is in red.

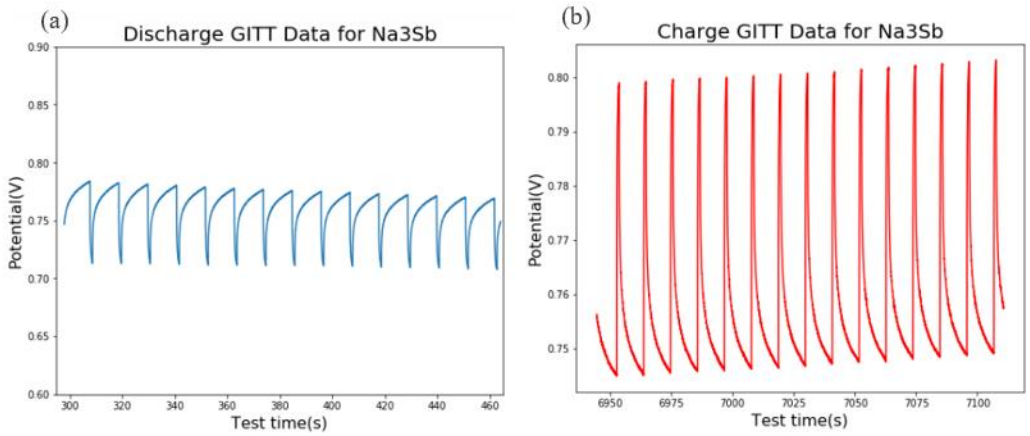

Figure 1.6 A zoomed in picture for the (a) discharge and (b) charge GITT data from Figure 1.5.

During the positive current pulse, the potential of the battery increases rapidly to a value which is proportional to the "iR" drop, where i is the current (A) and R is the summation of charge transfer resistance R_{ct} (Ω) and uncompensated resistance R_{un} (Ω). Due to the galvanostatic charge pulse, the battery potential starts to increase slowly to keep the concentration gradient constant. During the following relaxation time, the composition in the electrode becomes homogeneous due to diffusion of lithium ions. The potential then drops to a value which is proportional to the "iR" drop, and slowly decreases until it reaches both the equilibrium ($dE/dt \approx 0$) and the open circuit potential V_{oc} of the battery. This cyclic process of charge injection and relaxation continues until the battery is fully charged.

To perform GITT during battery discharge, the process is reversed. During the negative pulse, the potential of the battery decreases rapidly to a value which is proportional to the "iR" drop. Then, due to the galvanostatic charge pulse, the battery potential starts to decrease slowly to maintain the constant concentration gradient. During the relaxation time, due to the diffusion of the lithium ions, the potential increases quickly to a value which is proportional to the "iR" drop, and slowly increases until it reaches both the equilibrium and the open circuit potential V_{oc} of the battery. Again, this process is continuously repeated until the battery is fully discharged.

1.2.2 *Extracting Diffusion Coefficient from GITT Data through the Fickian GITT Diffusivity Model*

As mentioned in the previous section, GITT is a technique that can extract[12–20, 34–41] several thermodynamic and kinetic parameters of the battery. In this section, a traditional GITT diffusivity model[18] was used to determine the diffusion coefficients for the sodium ions in the sodium antimonide (Na_3Sb) system. By using the traditional GITT model, the potential changes are measured as a function of time. If the diffusion of sodium ions within the solid solution electrode is assumed to be one-dimensional without consideration of the ohmic potential drop, and the phase transformation is also neglected, then the diffusion coefficient can be determined by using the Fick's law through the following equation, which was proposed by John Wen and Robert Huggins in 1979.[18]

$$D_{GITT} = \frac{4}{\pi}\left(\frac{I V_M}{Z_A F S}\right)^2 \left[\frac{\left(\frac{dE(x)}{dx}\right)}{\left(\frac{dE(t)}{d\sqrt{t}}\right)}\right]^2 \qquad \left(t \ll \frac{L^2}{D_{GITT}}\right) \tag{1.1}$$

where L (cm) is the characteristic length of the electrode material, I (A) is the applied current, V_M (cm^3) is the molar volume of the electrode materials, Z_A is the charge number of element of the electrodes, F (C/mol) is the Faraday constant, and S (cm^2) is the contact surface area between the electrode and the electrolyte. In addition, the value of $dE(x)/dx$ can be determined by plotting the equilibrium voltage against the composition of the electrochemically active materials after each current pulse, and the value of $dE(t)/d\sqrt{t}$ can be determined by plotting the voltage against the square root of the time during constant current pulse.

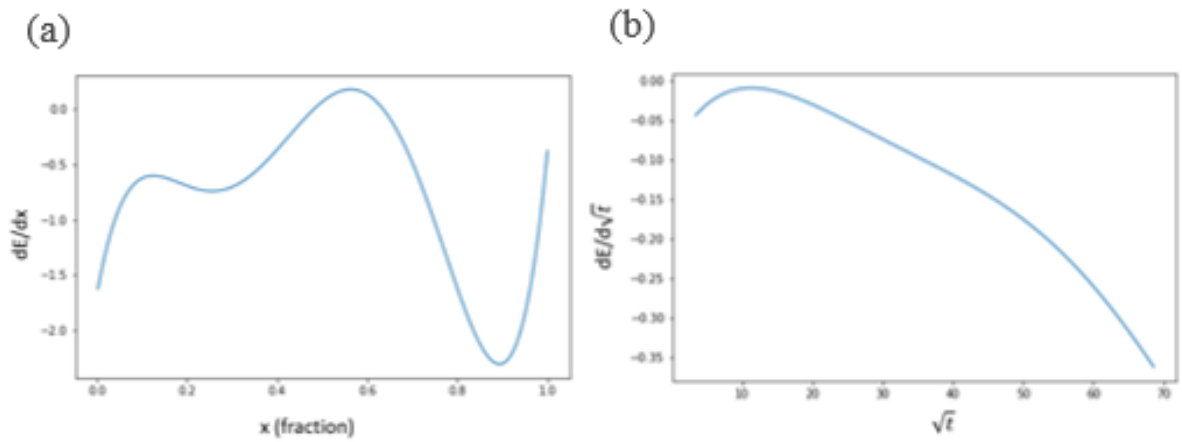

Figure 1.7. The curve of (a) $dE(x)/dx$ vs. x (ion fraction) (b) $dE(t)/d\sqrt{t}$ vs. $\sqrt{t}$.

With the constants and the associated physical properties of the antimony-based electrode materials, along with the two derivatives mentioned above, the diffusion coefficient can be determined through equation 1, and the diffusion coefficient profile is shown in Figure 1.8.

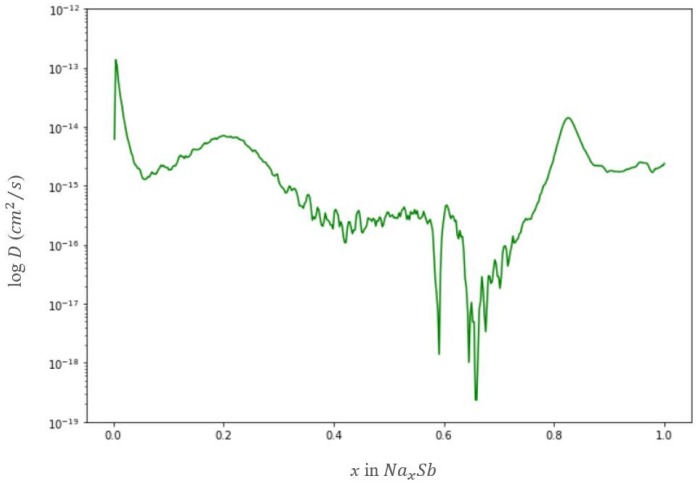

Figure 1.8. The calculated diffusion coefficient of the sodium ion at different sodium ion concentrations by using the standard GITT diffusivity model.

1.2.3 *A Novel Mixed Control Phase Transformation Model for Determining Diffusion Coefficients*

In Figure 1.8, the diffusion coefficients in the middle section ($0.05 < x < 0.8$) are 2-3 orders of magnitude lower than the diffusion coefficients at lower and higher concentrations of sodium in

Na_3Sb. Other studies[12,16–20] found a similar apparent drop in the diffusion coefficient profile in the lithium iron phosphate ($LiFePO_4$) system that this work extends upon. These discrepancies in the diffusion coefficient profile are because both Na_3Sb and $LiFePO_4$ are alloyed systems[21–25,50–52], in which there are phase transformations[53–57] occurring simultaneously with electrochemical reactions. To be more specific, in the Na_3Sb alloyed system, before the sodium ion diffuses, there is only the α phase throughout the whole system, which is the sodium ion poor phase. And after sodium ion starts to diffuse, some of the α phase start to transform to β phase, which is the sodium ion rich phase. Finally, when the sodium ion diffuses to a certain extent, all the α phase has been transformed, and only the β phase remains. Therefore, when both the α phase and the β phase exist in the system, we call this region the two-phase region, where the phase transformation happens. Moreover, the two-phase region is where the diffusion coefficient is relatively smaller than others when equation 1 is used.

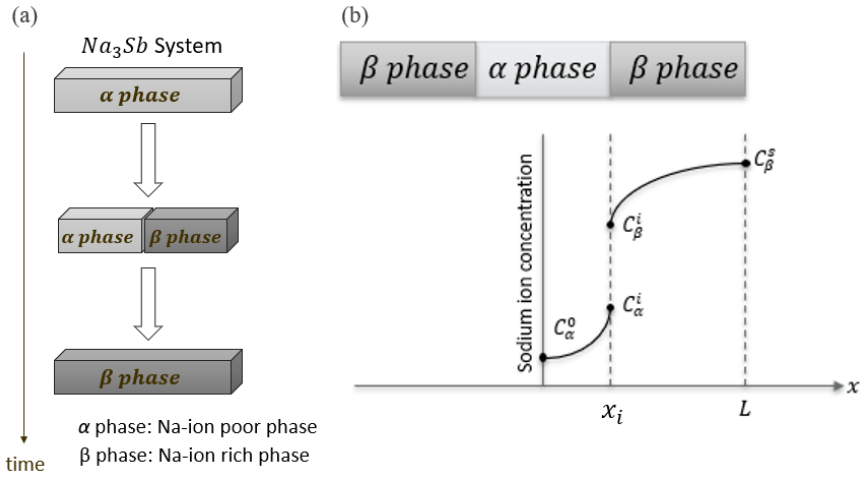

Figure 1.9. (a) The sodiation mechanism associated with inserting sodium ions into an alloying electrode material such as antimony. (b) An example of the concentration profile of the Na_3Sb system during the phase transformation associated with sodiation.

However, equation 1 is based on the Fick's Law, which assumes simple diffusion and does not take the phase transformation into account.[18] Therefore, it is not valid within the two-phase

region of phase transformation materials. In the two-phase region, both the interphase boundary and the ionic diffusion need to be considered at the same time. If the standard GITT diffusivity model is used, only an apparent diffusion coefficient[21–25] can be determined in the two-phase region, rather than the true diffusion coefficient.

To address the confounding phenomena of the interphase boundary and the ionic diffusion that occurs in standard GITT, a moving boundary model was proposed[23,58], which considers the interphase boundary within the two-phase region. However, the moving boundary model only considered diffusion as the main driving force and did not take the strain and stress associated with the phase transformation into account. Due to the omission of stress and strain at the interface, the diffusion coefficient in the two-phase region is still significantly lower than that in the single-phase region.[59]

Therefore, in order to take both the ionic diffusion as well as the mechanical stress at the interface into account simultaneously, a mixed control phase transformation theory was proposed by Yujie, *et al.*[14] The chemical and mechanical driving force on the interface and the kinetics within the moving boundary conditions during the phase transformation were determined. With this novel GITT diffusivity model, the true and precise diffusion coefficient in $LiFePO_4$ in the two-phase region were obtained, and can be validated by the diffusion coefficient in the single-phase regions determined by the standard GITT diffusivity model.

1.2.4 *Motivation of the Combination of GITT and Data Science*

Overall, GITT is a valuable technique for extracting several thermodynamic and kinetic parameters of a battery. In our group, we have focused on high-fidelity GITT[26], in which many data points are collected. Traditional GITT can include 10 to 20 datapoints per cycle while high-fidelity GITT can include hundreds of datapoints per cycle, which is more difficult to analyze using traditional

techniques. This represents an opportunity to leverage data science tools to build an analysis technique that can rapidly and automatically extract thermodynamic and kinetic parameters in the battery.

Herein, based on the novel mixed control phase transformation theory proposed by Yujie, *et al.*[14], a Python model was built to determine the diffusion coefficient in the two-phase region of our material Na_3Sb[26], an alloyed material. In addition, the calculation for the diffusion coefficients was clarified in more detail in this study, including the determination of the moving boundary conditions and the solution of the partial differential equations (PDEs). Moreover, based on Python programming, a user interface may be set up in the future to allow user to import the potential and composition data from GITT, and automatically extract the parameters in the battery.

Chapter 2. DATA SCIENCE APPROACHES FOR TOTAL DIFFERENTIAL CAPACITY PLOT ANALYSIS

The work presented in this chapter is the result of a collaborative training project[8] with Nicole Thompson, a graduated M.S. student in the Holmberg lab. Nicole developed this analysis and provided the Python codes for my Python programming training, including data cleaning, peak fitting, descriptor generation and the user interface.

The work within this chapter is in preparation for publication with permission from "N. L. Thompson *et al*., "DiffCapAnalyzer: A Python Package for Quantitative Analysis of Total Differential Capacity Data", *in preparation.*

2.1 PACKAGE REQUIREMENTS

In this analysis, there are 5 essential python files and 6 jupyter notebook files which demonstrate the codes and serve as documentations, which are shown in Tables 2.1 and 2.2.

Table 2-1. Essential Python files

	File name	Description
1	app_helper_functions.py	constructs the DASH based app imports the databasewrappers.py file and uses that file as the "connection" between the app and the data processing
2	chachifuncs.py	does the majority cleaning, calculates dQ/dV from raw files, and uses the databasefuncs.py file functions to save that cleaned data in the database
3	databasefuncs.py	updates and gets data from the database
4	databasewrappers.py	interacts with the database and the data processing
5	descriptors.py	gathers the descriptors from the model, including functions for peak finding, model fitting, sorting those descriptors for each peak, and saving those descriptors to the database

Table 2-2. Jupyter Notebook files

	File name	Description
1	chachifuncs.ipynb	documentations for chachifuncs.py
2	databasefuncs.ipynb	documentations for databasefuncs.py
3	databasewrappers.ipynb	documentations for databasewrappers.py
4	descriptors.ipynb	documentations for descriptors.py
5	process_data_example.ipynb	demonstrates the major work of this analysis
6	detailed_steps_example.ipynb	demonstrates the detailed work of the process_data_example.ipynb

In order to operate the analysis, users need to install several Python packages/modules, which are shown in Table 2.3 to 2.6, to run the functions successfully in the Python files mentioned above.

Table 2-3. Basic required packages

	Package/Module name	Description
1	glob	retrieves files/pathnames matching a specified pattern
2	itertools	provides various functions that work on iterators to produce complex iterators
3	math	a package contains several common mathematical functions
4	matplotlib	a comprehensive library for creating static, animated, and interactive visualizations in Python
5	numpy	provides a high-performance multidimensional array object, and tools for working with these arrays
6	os	provides a way of using operating system dependent functionality
7	pandas	offers data structures and operations for manipulating numerical tables and time series
8	sys	provides access to some variables used or maintained by the interpreter and to functions that interact strongly with the interpreter

Table 2-4. Required packages for processing data

	Package/Module name	Description
1	lmfit	a library for least-squares minimization and data fitting
2	peakutils	provides utilities related to the detection of peaks on 1D data
3	plotly	an interactive, open-source plotting library supporting over 40 unique chart types with a wide range of statistical, financial, geographic, scientific, and 3-dimensional use-cases
4	scipy	a free and open-source Python library used for scientific computing and technical computing

Table 2-5. Required packages for data management

	Package/Module name	Description
1	sqlite3	a Python standard library intended for working with SQLite3, a database engine

Table 2-6. Required packages for user interface

	Package/Module name	Description
1	ast	helps Python applications to process trees of the Python abstract syntax grammar
2	base64	provides data encoding and decoding as specified in RFC 3548
3	dash	an Open Source Python library for creating reactive, Web-based applications
4	io	provides Python's main facilities for dealing with various types of I/O
5	json	transfers data as text that can be sent over a network
6	requests	passes parameters in URLs to sending custom headers and SSL Verification
7	urllib	uses the urlopen function and is able to fetch URLs using a variety of different protocols

2.2 DATA SCIENCE WORKFLOW

In this analysis, the raw data is obtained from the database, smoothed through the data cleaning process, and fitted through peak deconvolution, which is followed by determining descriptors, and visualization of the final model through the user interface. In addition, documentations and demonstrations are included to make these codes more accessible. Figure 2.1 shows the data science workflow of this analysis.

Figure 2.1. Data science workflow for analysis of total differential capacity plots.

2.2.1 *Data Cleaning*

Before processing the data, it is important to clean the data and remove background noise. Figure 2.2 below shows an example of the raw data after calculating the dQ/dV curve. Clearly, there is noise and significant jumps in both the charge and discharges, which would result in misrepresentation of peak intensities and voltage shifts. To accurately identify and analyze the changes in electrochemical events over many cycles, it is essential to clean these features to obtain a clean peak profile.

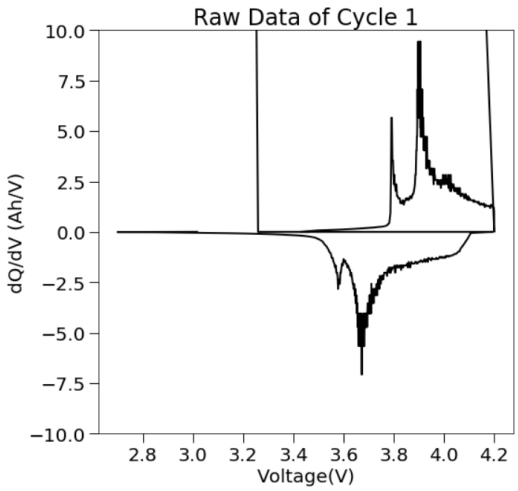

Figure 2.2. Raw data of cycle 1.

In order to eliminate noise and jumps, a function that can remove datapoints with $dV \approx 0$ is applied to the raw data, as shown in Figure 2.3.

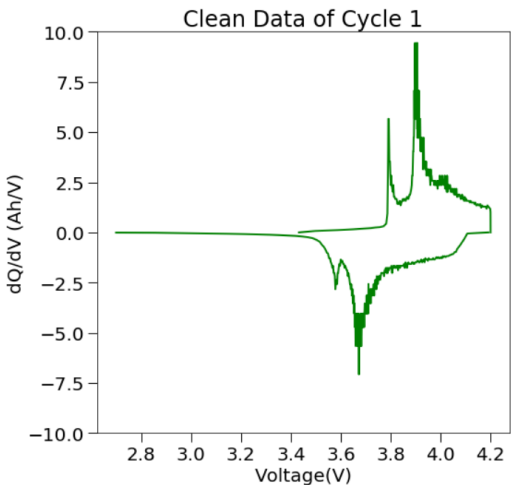

Figure 2.3. Data from cycle 1 after removing noise and spikes in data.

2.2.2 *Peak Fitting*

After eliminating the noise, a Savitzky–Golay filter[9] was applied to the clean data in order to achieve smooth data with clear peaks. A Savitzky–Golay filter is a digital filter that is often used for increasing the precision of the data without deforming the data tendency. Specifically, this filter is performing a process known as convolution, which fits consecutive sub-sets of adjacent data points. Those data points are fitted by the linear least squares method with low-degree polynomial, which is 3 in this analysis. Figure 2.4 shows the data after applying the Savitzky–Golay filter.

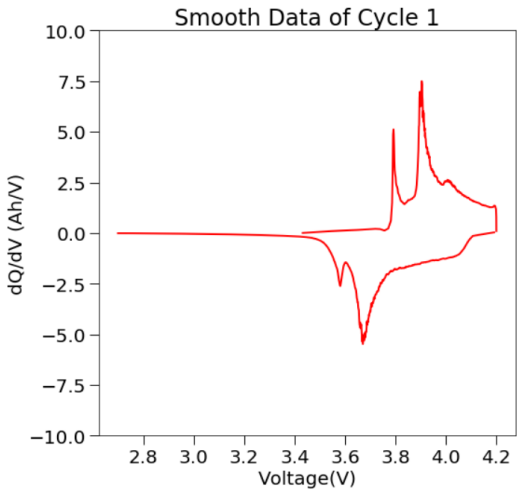

Figure 2.4. Smooth data after applying Savitzky–Golay filter on cycle 1.

The peakutils package is then applied to the charge and discharge cycle data to locate the peaks in these individual plots. *Peakutils* is a package that provides functions related to the detection of peaks on 1-dimensional data, including locating the indexes of peaks, estimating baselines, and performing Gaussian fits. Figure 2.5 shows the peak location of both a charge and discharge cycle.

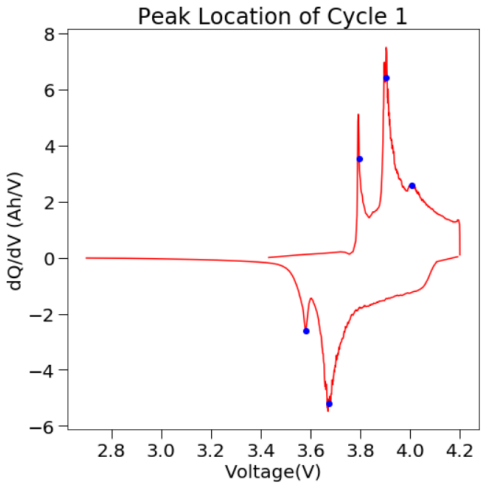

Figure 2.5. Peak locations identified for cycle 1.

Once the peaks are located, *lmfit* is applied to both the charge and discharge cycle data to generate models that fit the peaks. To elaborate, *lmfit* is an open-source fitting platform using a

Levenberg-Marquart algorithm, which is used to solve non-linear least squares problems, with numerically calculated derivatives. In this analysis, a mixture of Pseudo-Voigt distributions with a 4th degree polynomial background is fitted to the peak. The Pseudo-Voigt distribution has the following form:

$$\hat{f}(x) = \sum_{i=0}^{3} \hat{c}_i \, x^i + \sum_{j=1}^{n} \hat{f}_{v\,j}\,(x, \hat{A}_j, \hat{\mu}_j, \hat{\sigma}_j, \hat{\alpha}_j) \tag{2.1}$$

$$\sigma_g = \sigma/\sqrt{2ln2} \tag{2.2}$$

where $\hat{f}(x)$ is the function that fits the peaks, A is the amplitude of the peak, μ is the center of the distribution, σ and α are the fractions of Lorentzian character, and n is the number of peaks determined by the peak fitting function *peak_finder*, which is imported from the *peakutils* package.

Based on the peak located by the *peak_finder* function, *lmfit* package creates a 4th order polynomial fitting for the smoothed dataset. It begins by setting polynomial parameters based on a guess of a polynomial fit to the data with no peaks, which is shown as the "Initial Model" in Figure 2.6, and iterates over all peak indices until it reaches the best fitting model, which is shown as the "Fitted Model" in Figure 2.6.

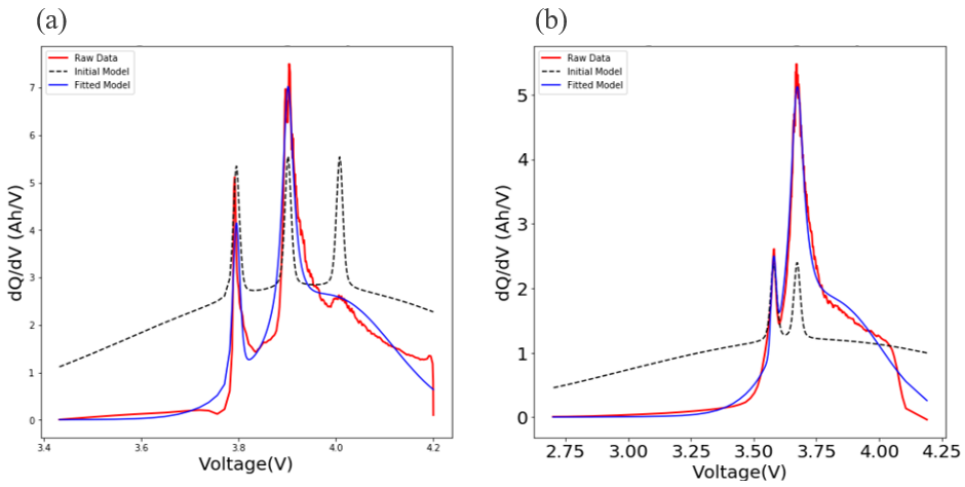

Figure 2.6. Peak fits of the (a) charge cycle 1 (b) discharge cycle 1, with the data (red), initial model (dotted), and fitted model (blue).

2.2.3 *Descriptor Generation*

Once the model is finished, the generated model is processed to generate a dictionary that stores the information of the peaks, including coefficients of the fitting curve, error parameters, the height of peak (dQ/dV), the location of peak (V), and the standard deviation of the peak (σ). Then, it iterates this process to store the information, including the heights and the locations, of all the peaks, and label all the peaks along with their corresponding clean cycle data, which is shown in Table 2.7.

Table 2-7. Descriptors of charge cycle 1

Height of peak (dQ/dV)	3.5463	6.43033	2.5843
Location of peak (V)	3.7958	3.9020	4.0079

Finally, the heights and locations of the peaks over a range of cycle numbers can be plotted. For example, the peak locations and heights of the charge cycle in Figure 2.7 and the 2.8, respectively.

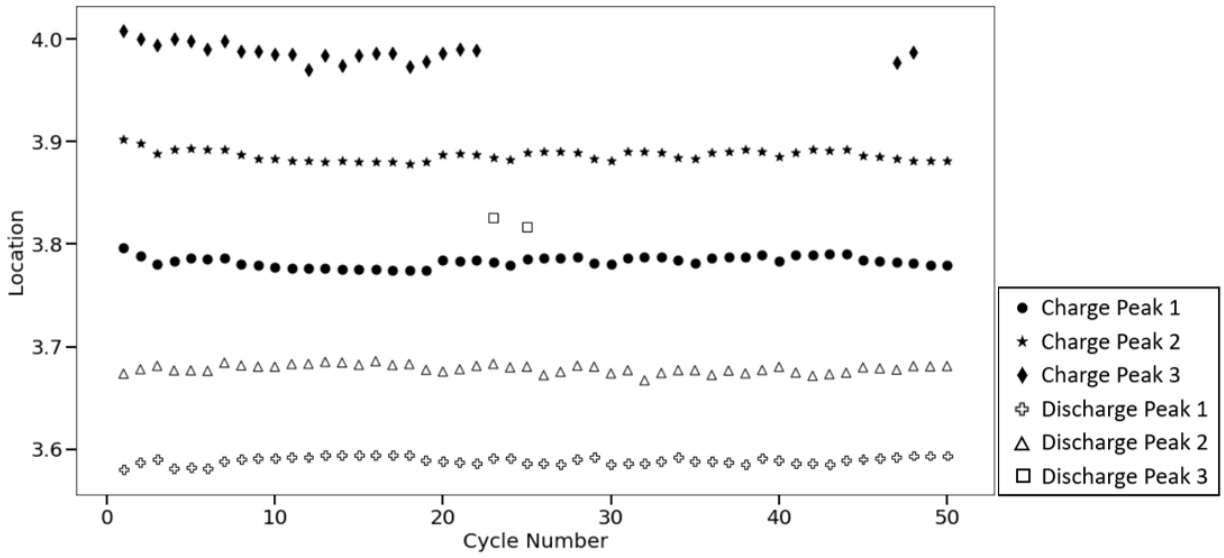

Figure 2.7. The peak locations of the charge cycle over a range of cycle numbers.

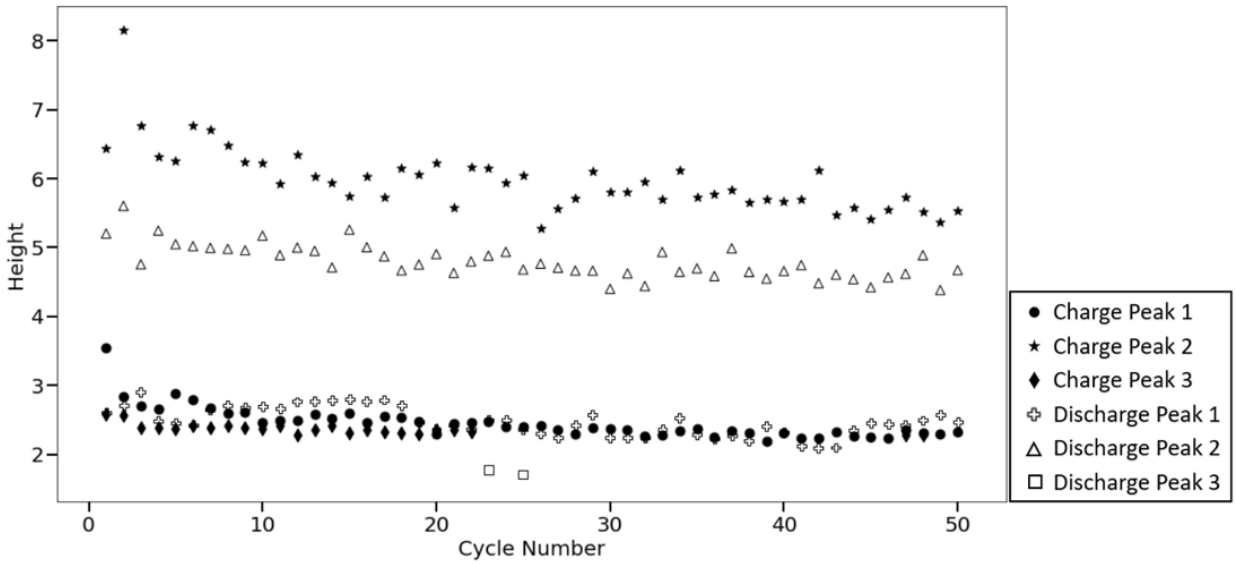

Figure 2.8 The peak heights of the charge cycle over a range of cycle numbers.

2.3 MODEL AND DOCUMENTATIONS

2.3.1 *User Interface*

To visualize this analysis, an interface has been set up for the user easily see the process of cleaning, peak fitting and obtaining descriptors. This is a DASH-based visualization application (app) that can be used as the user interface. Users can upload raw cycling data, either collected through a MACCOR or an Arbin cycler. The app will then process the data and add a few files to the database, including the raw data, the clean data, and the peak descriptors for every cycle. The app also allows users to scroll through cycles and better understand the differential capacity curves. Additionally, there is a section to evaluate the fit of the gaussian baseline and tailor the peak finding process. The user can also download the peak descriptors using the "Download CSV" file button in the app. Figure 2.9 is the preview of the user interface.

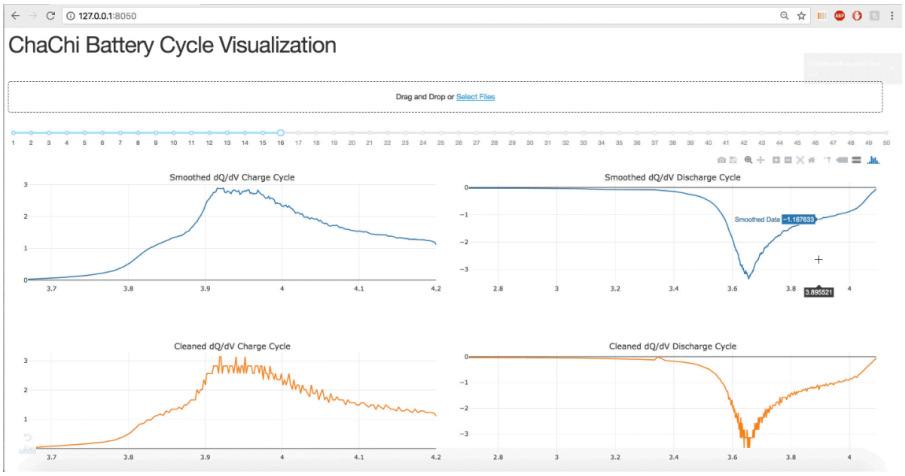

Figure 2.9. A preview of the user interface.

2.3.2 *Documentations and Demonstrations*

In addition to developing users visualize the work of this analysis, additional documentations have also been established to help users understand the code more easily. In the "Data-Science-Approaches-for-Total-Differential-Capacity-Plot-Analysis" repository on GitHub (https://github.com/cwh32/Data-Science-Approaches-for-Total-Differential-Capacity-Analysis), both the essential Python files and the user interface have been uploaded. In addition, some Jupyter notebooks have been set up as the documentations, which detail the applications of all the functions as well as clarify the required inputs for the users. As an example shown in Figure 2.10, the definition of the "drop_0_dv" function is explained, and followed by the clarification of the input variables. By documenting all the functions in this code, we aim to help users to understand how each function works to make this code as accessible as possible.

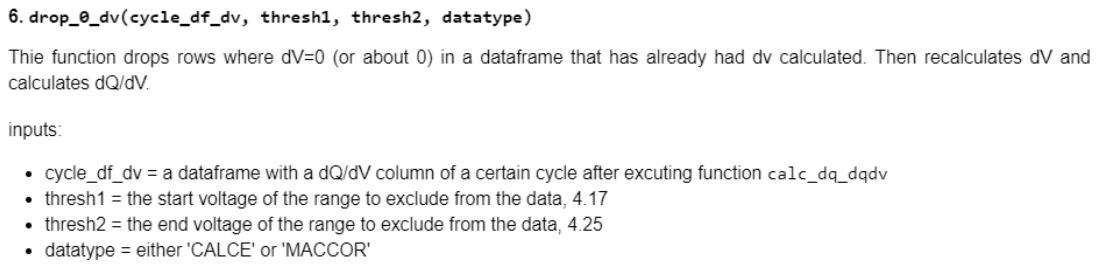

Figure 2.10. An example of the documentation, describing the purpose of the function as well as the relevant inputs.

In addition to the documentations of the code, tutorials have been set up within Jupyter notebooks to illustrate how to use each function to process the data step-by-step. These notebooks demonstrate each of the process, ranging from importing the raw data from the database to generating the descriptors for the peaks. With these documentations and tutorials, the accessibility of the automated differential capacity analysis has been improved.

2.4 FUTURE DIRECTIONS

There are a number of areas where our quantitative total differential capacity analysis tool could be improved. First of all, there is room to generalize the input data more, so that more types of batteries can be used. Currently, this analysis is restricted to a specific format, with specific column headers. Users can only upload the data either collected through MACCOR or Arbin cycler; files that are not in these two formats cannot be processed through this analysis. Therefore, the code can be rewritten to recognize the needed information and extract it from the input data in any kind of format, for example, using the voltage data. Consequently, with the adjustment proposed above, users could upload the input data of more different types of battery cyclers.

Second, sometimes the peak_finder package is too sensitive in peak locating, which means that it labels a peak where is not a peak. This issue can be addressed by adjusting the parameters

in the peak_finder function. However, this adjustment is still manual currently, which may decrease the accuracy of the peak_finder function. Therefore, if a model can be set up to evaluate the accuracy of peak locating automatically, then there will no need for the user to adjust the parameters by themselves.

For the documentation and the demonstrations part, more commenting can be added to help users familiarize themselves with the codes, especially for uses who are not familiar with Python programming. With those changes and adjustment mentioned above, this differential capacity plot analysis along with the corresponding documentation and demonstration can be a more powerful, standardized, and accessible tool in battery cycling data analysis.

Chapter 3. GITT METHOD FOR DETERMINING DIFFUSION COEFFICIENTS DURING PHASE TRANSFORMATIONS

The work presented in this chapter is the result of a collaborative project with Dr. Grant Williamson[26] from the Holmberg lab. Grant has provided the GITT data of Na_3Sb, and we worked closely together to study the electrochemistry and extract the thermodynamic and kinetic parameters of the electrode materials.

The data included in this chapter is intended to be published in a peer reviewed journal by "Grant Williamson *et al.* [26]" and is subject to their license restrictions.

3.1 GALVANOSTATIC INTERMITTENT TITRATION TECHNIQUE

As mentioned in the introduction section, the focus of this study is on developing methods to calculate the diffusion coefficients for electrode materials that undergo both a chemical transformation during cycling as well as a significant volume expansion during phase transformation. In order to extract these parameters, this required the determination of moving boundary conditions and the solving PDEs. As a result, this chapter will cover those calculations in detail.

3.1.1 *Kinetics during Phase Transformation*

In the mixed control phase transformation theory[14], the concentration profile and the diffusion coefficients can be determined by solving the set of PDEs from Fick's 2nd Law[60,61] with a moving interface boundary condition. The theoretical concentration profile of the sodium-ion during the discharge process is shown in Figure 1.9b. The boundary between α (working-ion-poor phase) and β (working-ion-rich phase) phases is moving to the position x_i corresponding to the composition of the working ion in the electrode. With the mixed control phase-transformation theory, the

concentration profile of working-ion in both α and β phases, and corresponding initial and boundary conditions can be expressed as follows,

In the α phase

$$\frac{\partial C_\alpha}{\partial t} = D_\alpha\left(\frac{\partial^2 C_\alpha}{\partial x^2}\right) \tag{3.1}$$

$$C_\alpha = C_\alpha^0 \qquad t = 0 \tag{3.2}$$

$$\frac{\partial C_\alpha}{\partial x} = 0 \quad x = 0,\ t \geq 0 \tag{3.3}$$

In the β phase

$$\frac{\partial C_\beta}{\partial t} = D_\beta\left(\frac{\partial^2 C_\beta}{\partial x^2}\right) \tag{3.4}$$

$$C_\beta = C_\beta^0 \quad t = 0 \tag{3.5}$$

$$C_\beta = C_\beta^s \quad x = L \tag{3.6}$$

where C_α and C_β are the concentration profiles of the working-ion in α and β phases respectively, D_α and D_β are the diffusion coefficients of the working-ion in α and β phases respectively, C_α^0 and C_β^0 are the initial concentrations of working ion in α and β phase respectively, C_β^s is the concentration at the end of β phase. By solving the PDEs above, the concentration profile in the α and β phase can be obtained, and hence, the corresponding diffusion coefficients can be determined. However, along with the boundary and the initial conditions above, it still requires the boundary conditions on the interface for both α and β phase. Therefore, the following sections will illustrate how to determine the position and the concentration on the interface.

3.1.2 *Chemical and Mechanical Driving Forces on the Interface*

In order to take the moving boundary into account, the driving forces on the interface[62–65] needed to be considered. The driving force G[66–69] can be expressed as follow,

$$\Delta G = \Delta G_{chem} + \Delta G_{accom} + \Delta G_{int} \tag{3.7}$$

where ΔG_{chem} is the chemical driving force, ΔG_{accom} is the accommodation energy, and ΔG_{int} is the interface energy[70,71], which can be neglected due to the assumption of planar interface in this study.

In the phase transformation process, the sodiation and the desodiation reactions can be expressed as follows,

$$Na_ySb + (z-y)Na^+ + (z-y)e^- \xrightarrow{sodiation} Na_zSb \tag{3.8}$$

$$Na_ySb + (z-y)Na^+ + (z-y)e^- \xleftarrow{desodiation} Na_zSb \tag{3.9}$$

where y is the composition of the sodium-ion in Na_ySb, and z is the mole fraction of sodium-ion in the β phase.

During the sodiation process, the molar chemical driving force ΔG_{chem} can be determined by the summation of the difference of the chemical potentials between α and β phase, which is shown as follows,

$$\Delta G_{chem} = z\left(\mu^{\beta}_{Na^+} - \mu^{\alpha}_{Na^+}\right) + (1-z)\left(\mu^{\beta}_{Sb^{3-}} - \mu^{\alpha}_{Sb^{3-}}\right) \tag{3.10}$$

due to the higher mobility of sodium ions, and the assumption of the extremely thin interface, the chemical potential of the sodium ions between α and β phase can be expressed as follow,

$$\mu^{\alpha}_{Na^+} = \mu^{\beta}_{Na^+} \tag{3.11}$$

which means that the chemical potential across the interface is continuous, leading to the assumption of a relationship between the concentration of sodium-ion in the α and β phase on the interface.[72] To elaborate, this relationship between these two concentrations can be obtained by extrapolating the equilibrium potential lines, and the actual interfacial sodium-ion concentration of α and β phase (C^i_α and C^i_β) can be determined by the intersection of the equilibrium potential line and GITT potential data in α and β phase. From Figure 3.1(a)[73], the sodium ion concentration

on the moving interface of α and β phase (C_α^i and C_β^i) is obtained by the intersection of the equilibrium potential of the α/β interface during discharge with a-b and c-d lines.

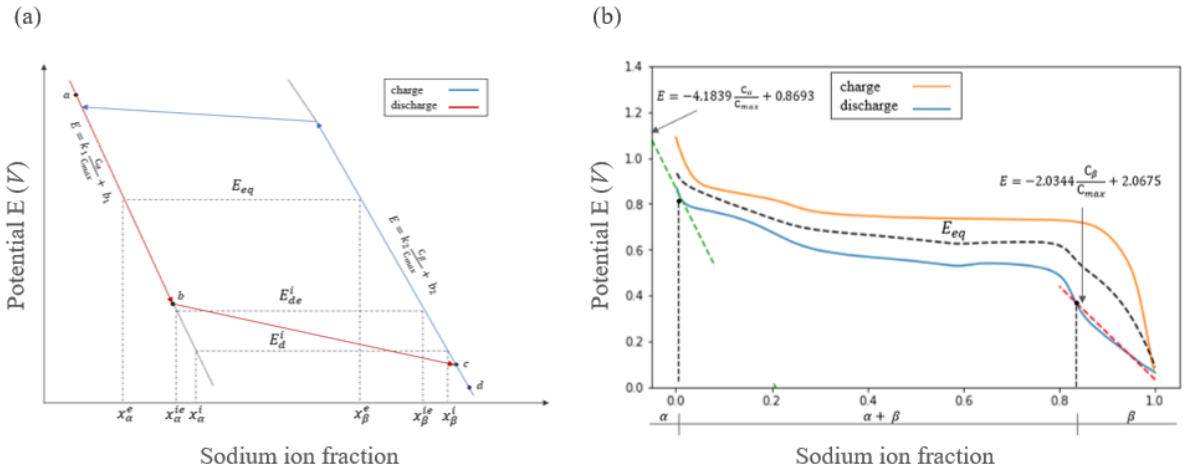

Figure 3.1. A potential vs. composition isotherm from (a) theory, with charge (blue) and discharge (red) cycles and (b) GITT data, with charge (orange) and discharge (blue) cycles. The dotted line represents the isotherm associated with the equilibrium potential.

On the other hand, the chemical potentials of antimony ion at the interface are not the same, which means that $\mu_{Sb^{3-}}^{\alpha} \neq \mu_{Sb^{3-}}^{\beta}$, leading to drive the α phase lattice to transform to the β phase lattice. In order to determine the chemical potential at the interface ΔG_d^i, the Nernst equation is applied here,

$$\Delta G_d^i = -(z-y)FE_d^i \tag{3.12}$$

$$z = \frac{C_\beta^i}{C_{max}} \tag{3.13}$$

$$y = \frac{C_\alpha^i}{C_{max}} \tag{3.14}$$

where z is the mole fraction of sodium-ion in β phase, y is the mole fraction of sodium ion in α phase, C_{max} is the maximum concentration of sodium ion in this system, which is the reciprocal to the molar volume of sodium antimonide. Likewise, the Gibbs free-energy change for the sodiation reaction (equation 3.8) can be determined as follows,

$$\Delta G_{eq} = -\left(\frac{C_\beta^e - C_\alpha^e}{C_{max}}\right) F E_{eq} \tag{3.15}$$

where E_{eq} is the theoretical potential (strain-free), C_α^e and C_β^e are the theoretical sodium-ion solubility in the α and β phase corresponding to E_{eq}. Therefore, by determining the difference between the chemical potential at the interface ΔG_d^i and the Gibbs free-energy change for the sodiation reaction ΔG_{eq}, the chemical driving force ΔG_{chem} can be expressed as follows,

$$\Delta G_{chem} = \left(\frac{C_\beta^i - C_\alpha^i}{C_{max}}\right) F E_d^i - \left(\frac{C_\beta^e - C_\alpha^e}{C_{max}}\right) F E_{eq} \tag{3.16}$$

In order to determine the accommodation energy ΔG_{accom}, the elastic-plastic strain during the phase-transformation process needs to be considered. Because of the elastic-plastic strain, the α and β phases will be equilibrium at a lower equilibrium potential E_{de}^i instead of the equilibrium potential E_{eq} to balance the strain-induced accommodation energy. In the same manner, the accommodation energy ΔG_{accom} can also be calculated by the difference of the chemical free energy,

$$\Delta G_{accom} = \left(\frac{C_\beta^e - C_\alpha^e}{C_{max}}\right) F E_{eq} - \left(\frac{C_\beta^{ie} - C_\alpha^{ie}}{C_{max}}\right) F E_{de}^i \tag{3.17}$$

where C_α^{ie} and C_β^{ie} are the equilibrium interfacial sodium ion concentration in the α and β phases corresponding to E_{de}^i, and E_{de}^i is the actual equilibrium potential of the electrode during the discharge process, which can be obtained from the GITT data. Because the accommodation energy will accumulate along the *x* direction, ΔG_{accom} can be considered as a function of position x_i, and equation 3.17 can be expressed as follows,

$$\Delta G_{accom} = \left(\frac{C_\beta^e - C_\alpha^e}{C_{max}}\right) F E_{eq} - \left(\frac{C_\beta^{ie} - C_\alpha^{ie}}{C_{max}}\right) F E_{de}^i = f(x_i) \tag{3.18}$$

Therefore, the total driving force ΔG_d can be determined by combining equation 3.16 and 3.18, which can be expressed as follows,

$$\Delta G_d = \Delta G_{chem} + \Delta G_{accom} = \left(\frac{C_\beta^i - C_\alpha^i}{C_{max}}\right) FE_d^i - \left(\frac{C_\beta^{ie} - C_\alpha^{ie}}{C_{max}}\right) FE_{de}^i \quad (3.19)$$

or it can also be expressed as a function of position x_i,

$$\Delta G_d = \Delta G_{chem} + \Delta G_{accom} = \left(\frac{C_\beta^i - C_\alpha^i}{C_{max}}\right) FE_d^i - \left(\frac{C_\beta^e - C_\alpha^e}{C_{max}}\right) FE_{eq} + f(x_i) \quad (3.20)$$

Before the determination of the accommodation energy $f(x_i)$ in equation 3.18, the theoretical (strain-free) equilibrium potential E_{eq} can be approximately estimated as the average of charge equilibrium potential E_{ce} and discharge equilibrium potential E_{de}, and similarly, C_α^e, C_β^e, C_α^{ie} and C_β^{ie} can be determined by plugging E_{eq} and E_{de}^i into equation 3.21 to 3.24.

$$E_{eq} = k_1 \frac{C_\alpha^e}{C_{max}} + b_1 \quad \text{(for the } \alpha \text{ phase)} \quad (3.21)$$

$$E_{eq} = k_2 \frac{C_\beta^e}{C_{max}} + b_2 \quad \text{(for the } \beta \text{ phase)} \quad (3.22)$$

$$E_{de}^i = k_1 \frac{C_\alpha^{ie}}{C_{max}} + b_1 \quad \text{(for the } \alpha \text{ phase)} \quad (3.23)$$

$$E_{de}^i = k_2 \frac{C_\beta^{ie}}{C_{max}} + b_2 \quad \text{(for the } \beta \text{ phase)} \quad (3.24)$$

Subsequently, the accommodation energy can be determined by plugging those concentrations above into equation 3.18, and the calculated accommodation energies at the different sodium ion concentration in Figure 3.2 were fitted with a 3rd order polynomial function $f(x_i)$, which is shown as a solid line in Figure 3.2.

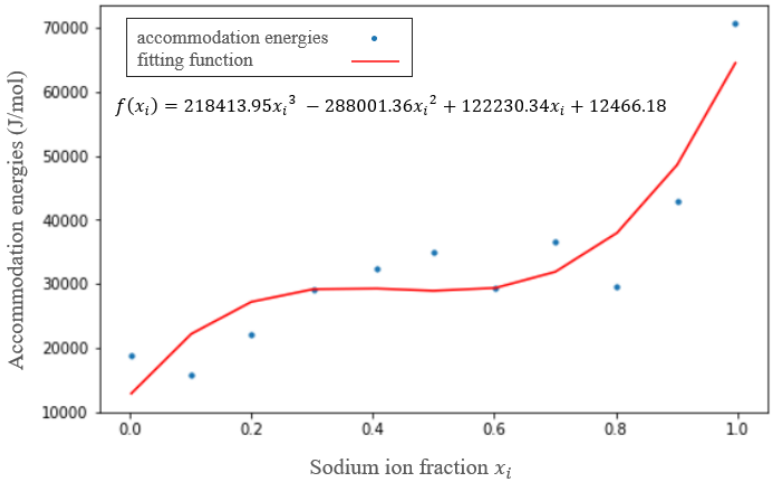

Figure 3.2. Discharge accommodation energies as a function of sodium ion concentration and the corresponding fitting function.

Once the accommodation energy is determined, it can be plugged into equation 3.20, and therefore, the driving force on the interface can be obtained.

3.1.3 *Interface Boundary Conditions Determination*

In order to determine the boundary conditions of the interface, the position of the interface can first be calculated from integrating the interface velocity. In equation 3.25, the interface velocity can be obtained by the driving force ΔG_d multiplied by the interface mobility M[73] (m mol (J s)).

$$\frac{dx_i(t)}{dt} = M\Delta G_d \tag{3.25}$$

Therefore, by integrating both sides of equation 3.22, the position of the interface can be obtained, as shown in equation 3.26 and Figure 3.3.

$$x_i(t) = \int M\Delta G_d \, dt + constant \tag{3.26}$$

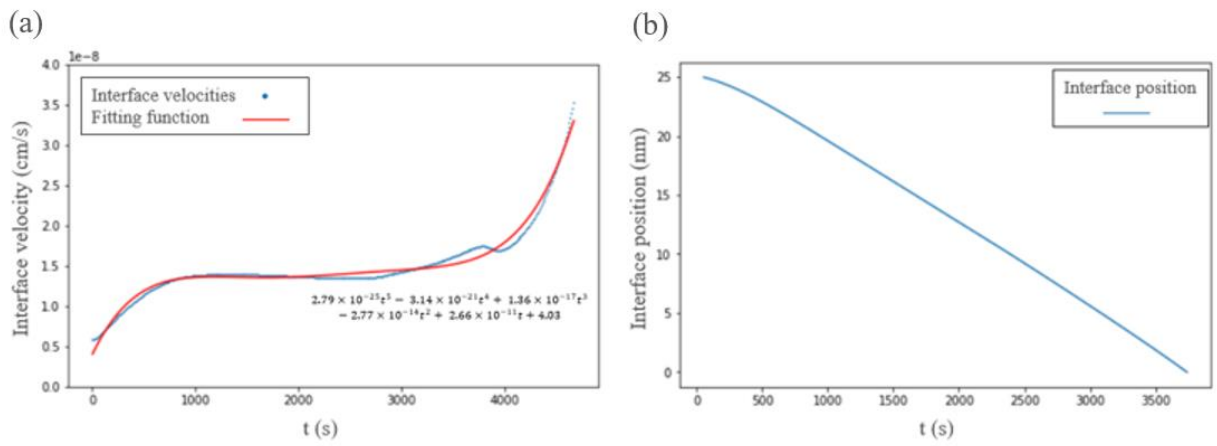

Figure 3.3. Profile of the (a) interface velocity, with calculated data (blue) and fitted curve (red) and (b) interface position as a function of time.

Once the position of the interface is obtained, the next step of the calculation is to determine the concentration information at the interface. From Figure 3.1, the actual interfacial sodium ion concentration (C_α^i and C_β^i) can be determined by the intersection of the equilibrium potential line and GITT potential data in α and β phase. Therefore, C_α^i and C_β^i can be obtained by plugging the actual potential of the α/β interface (E_d^i) into equation 3.27 and 3.28, which are shown as follows:

$$E_d^i = k_1 \frac{C_\alpha^i}{C_{max}} + b_1 \qquad \text{(for the } \alpha \text{ phase)} \qquad (3.27)$$

$$E_d^i = k_2 \frac{C_\beta^i}{C_{max}} + b_2 \qquad \text{(for the } \beta \text{ phase)} \qquad (3.28)$$

where k_1 and k_2 are the slopes of the solubility versus equilibrium potential lines in the α and β single phase and b_1 and b_2 are the intercepts. Therefore, with the position of the interface between the α and β phase and the corresponding concentration information, the PDEs for both C_α and C_β can be solved by the addition of a second boundary condition, which is shown in equation 3.29 and 3.30.

$$C_\alpha = C_\alpha^i \quad x = the\ interface\ position,\ t \geq 0 \qquad (\alpha \text{ phase}) \qquad (3.29)$$

$$C_\alpha = C_\beta^i \quad x = the\ interface\ position,\ t \geq 0 \qquad (\beta \text{ phase}) \qquad (3.30)$$

After both the initial conditions and boundary conditions of the PDEs are determined, the PDEs can then be solved.

In addition to the boundary conditions determined above, Table 3.1 shows a summary of the parameters used for the following PDE calculations.

Table 3-1. Parameters used for PDE calculations

Parameters	
particle size (nm)	25
molar volume of Na_3Sb (cm^3/mol)	18.18 ~ 73.24
C_{max} (mol/cm^3)	0.013888889
k_1 and k_2	-4.1839 and -2.0344
b_1 and b_2	0.8693 and 2.0675
Interface mobility *M* (cm mol/(J s))	5.57×10^{-13}
Faraday constant *F* (C/mol)	96500
applied current *I* (A)	7×10^{-5}
charge number Z_A	1
contact area between the electrode and electrolyte *S* (cm^2)	1.76715

3.2 NUMERICAL METHOD THROUGH PYTHON

In order to approximate the differential terms in the PDEs[31–33], the finite difference method (FDM) was applied. In the explicit method of the FDM, the governing equation of the PDEs, equation 3.1 and 3.4 can be approximated as follows,

$$\frac{C_{\alpha_j}^{n+1} - C_{\alpha_j}^{n}}{k} = D_\alpha\left(\frac{C_{\alpha_{j+1}}^{n} - 2C_{\alpha_j}^{n} + C_{\alpha_{j-1}}^{n}}{h^2}\right) \tag{3.31}$$

$$\frac{C_{\beta_j}^{n+1} - C_{\beta_j}^{n}}{k} = D_\beta\left(\frac{C_{\beta_{j+1}}^{n} - 2C_{\beta_j}^{n} + C_{\beta_{j-1}}^{n}}{h^2}\right) \tag{3.32}$$

where *k* and *h* are the time and space interval, *n* and *j* are the indices for each time and space steps, respectively.

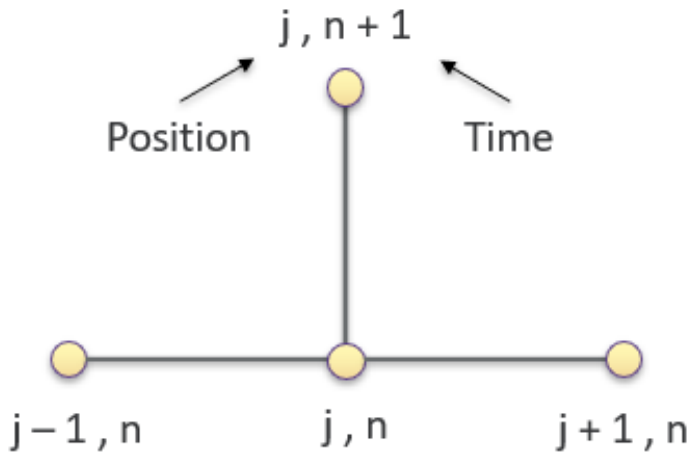

Figure 3.4. The idea of the explicit method of the finite difference method.

Therefore, the recurrence relation for C_α and C_β can be expressed in equation 3.33 to 3.36.

$$C_{\alpha_j}^{n+1} = (1 - 2\varepsilon)C_{\alpha_j}^{n} + \varepsilon C_{\alpha_{j-1}}^{n} + \varepsilon C_{\alpha_{j+1}}^{n} \tag{3.33}$$

$$C_{\beta_j}^{n+1} = (1 - 2\delta)C_{\beta_j}^{n} + \delta C_{\beta_{j-1}}^{n} + \delta C_{\beta_{j+1}}^{n} \tag{3.34}$$

$$\varepsilon = \frac{D_\alpha \times k}{h^2} \tag{3.35}$$

$$\delta = \frac{D_\beta \times k}{h^2} \tag{3.36}$$

By solving the above PDEs with the corresponding boundary and initial conditions, the profile of the concentration in the α and β phase C_α and C_β can be determined, and the corresponding diffusion coefficients D_α and D_β can be obtained.

3.3 Results and Conclusion

3.3.1 *Results*

Figure 3.5 shows the concentration profiles of sodium ions in the $\alpha + \beta$ region over distance, where each curve represents a different time point.

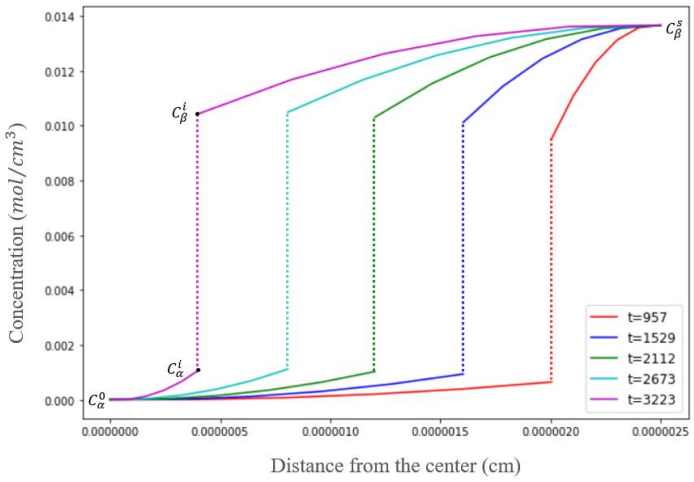

Figure 3.5. Concentration profiles of sodium ions in the $\alpha + \beta$ region.

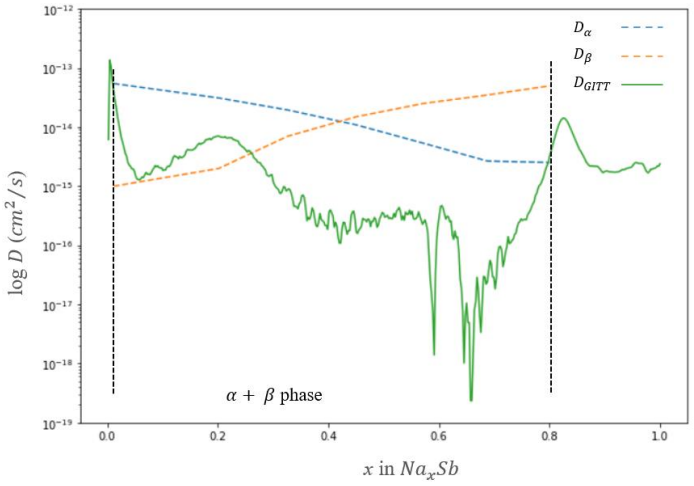

Figure 3.6. Diffusion coefficients in $\alpha + \beta$ region.

The diffusion coefficients D_α and D_β were also plotted versus the sodium ion fraction in Na_xSb, as shown in Figure 3.6. For comparison, the diffusion coefficients calculated through the standard GITT diffusivity model D_{GITT} were also plotted in Figure 3.6. Similar to the results from other studies[12,16–20], those D_{GITT} calculated in the $\alpha + \beta$ region are 2-3 orders of magnitude lower than those in the single-phase region. The results of the standard GITT diffusivity model are not reasonable, not only because the single-phase assumption of the two-phase region is not valid, as mentioned in the introduction, but also because the composition and structure of the α phase does

not change after the deposition of β phase, D_α should not drop in the $\alpha+\beta$ region.[14] As the diffusion coefficient D_{GITT} in the single-phase regions ($0 < x_i < 0.01, 0.8 < x_i < 1$) is reliable, the mixed control phase-transformation method can be validated[47] by the similarity between D_{GITT} in the single-phase regions and D_α and D_β in the two phase region. In Figure 3.6, the diffusion coefficient of the α and β single phase is about 10^{-15}-$10^{-14} cm^2/s$ and 10^{-17}-$10^{-15} cm^2/s$ respectively; and the diffusion coefficient D_α and D_β in the $\alpha+\beta$ region is about 10^{-15}-$10^{-13} cm^2/s$ and 10^{-16}-$10^{-13} cm^2/s$, respectively. The diffusion coefficient D_α decreases slightly through the $\alpha+\beta$ region, which may be attributed to the gradually reduced total length of the sodium ion diffusion as well as the increase of the actual interface sodium ion concentration C_α^i, which is also a boundary condition of the PDEs. Likewise, the diffusion coefficient D_β increases slightly through the $\alpha+\beta$ region, which is due to the gradually increased total length of sodium ion diffusion and the reduced concentration difference between C_β^i and C_β^s. Overall, only one apparent diffusion coefficient profile in the two-phase region can be obtained by using the standard GITT diffusivity model, but with the mixed control phase-transformation method, diffusion coefficient profiles in both α and β phases in the two-phase region can be determined.

3.3.2 *Conclusion*

Phase-transformation GITT methods were developed based upon the mixed-control phase-transformation theory, which takes chemical driving forces, mechanical driving forces, and the kinetics associated with the moving boundary into account. By solving the PDEs in both α and β phase with the corresponding initial and moving boundary conditions, the concentration profiles C_α and C_β in the two-phase region were determined. Therefore, the true diffusion coefficient in the α and β phases were obtained and the unreasonable drop of the apparent diffusion coefficient

in the two-phase region could be corrected. In addition, these results also validate that this novel mixed control phase transformation model can be applied to various types of electrochemically active alloying materials, including the $LiFePO_4$ system from Yujie, *et al.* and the Na_3Sb system in this study.

3.4 Future Directions

As mentioned in the introduction because the method proposed above is built upon Python programming, it can be easily extended to add a user interface. Users can then upload battery cycling data collected through GITT, and the user interface can extract the thermodynamic and kinetic information of the battery through performing the calculation described above.

Furthermore, there are only 5 sets of PDEs that were solved in the above method currently, which is shown in the Figure 3.5. Therefore, by performing more sets of PDE calculations, the accuracy of the diffusion coefficients in the two-phase region can be improved. To be more specific, a function can be set up to perform the PDE solving automatically, and at the same time, users can determine how many sets of PDEs they want to solve in order to avoid the long waiting time for the computer's calculation. In the same manner, users can also adjust the number of steps in the finite difference method. By setting up the user interface and implementing these adjustments, it is hoped that the user can obtain the information of the battery more precisely and accessibly.

REFERENCES

1. Beck, D. A. C., Carothers, J. M., Subramanian, V. R. & Pfaendtner, J. Data science: Accelerating innovation and discovery in chemical engineering. *AIChE J.* (2016) doi:10.1002/aic.15192.
2. Dehmer, M., Varmuza, K. & Bonchev, D. *Statistical Modelling of Molecular Descriptors in QSAR/QSPR*. *Statistical Modelling of Molecular Descriptors in QSAR/QSPR* (2012). doi:10.1002/9783527645121.
3. Dean, J. & Ghemawat, S. MapReduce: Simplified data processing on large clusters. *Commun. ACM* (2008) doi:10.1145/1327452.1327492.
4. Venkatasubramanian, V. Drowning in data: Informatics and modeling challenges in a data-rich networked world. *AIChE J.* (2009) doi:10.1002/aic.11756.
5. Codd, E. F. A Relational Model of Data for Large Shared Data Banks. *Commun. ACM* (1983) doi:10.1145/357980.358007.
6. Christophersen, J. P. *et al. Advanced technology development program for lithium-ion batteries: Gen 2 performance evaluation final report*. *Idaho National …* (2006).
7. Christophersen, J. P. & Shaw, S. R. Using radial basis functions to approximate battery differential capacity and differential voltage. *J. Power Sources* (2010) doi:10.1016/j.jpowsour.2009.08.094.
8. Thompson, N., & Holmberg, Vincent Carl. (2018). *Total differential capacity plot analysis using data science methods*. Seattle]: University of Washington.
9. Weng, C., Cui, Y., Sun, J. & Peng, H. On-board state of health monitoring of lithium-ion batteries using incremental capacity analysis with support vector regression. *J. Power Sources* (2013) doi:10.1016/j.jpowsour.2013.02.012.
10. Aihara, Y. *et al.* The electrochemical characteristics and applicability of an amorphous sulfide-based solid ion conductor for the next-generation solid-state lithium secondary batteries. *Front. Energy Res.* (2016) doi:10.3389/fenrg.2016.00018.
11. Wan, J. *et al.* Galvanostatic Intermittent Titration Technique. *Sci. China Technol. Sci.* (2016) doi:10.1007/s11431-016-6052-z.
12. Deiss, E. Spurious chemical diffusion coefficients of Li+ in electrode materials evaluated with GITT. *Electrochim. Acta* (2005) doi:10.1016/j.electacta.2004.11.042.
13. Tang, K., Yu, X., Sun, J., Li, H. & Huang, X. Kinetic analysis on LiFePO4 thin films by CV, GITT, and EIS. *Electrochim. Acta* (2011) doi:10.1016/j.electacta.2011.02.119.
14. Zhu, Y. & Wang, C. Galvanostatic intermittent titration technique for phase-transformation electrodes. *J. Phys. Chem. C* (2010) doi:10.1021/jp9113333.
15. Mao, Z., Farkhondeh, M., Pritzker, M., Fowler, M. & Chen, Z. Dynamics of a Blended Lithium-Ion Battery Electrode During Galvanostatic Intermittent Titration Technique. *Electrochim. Acta* (2016) doi:10.1016/j.electacta.2016.11.169.
16. Ding, N. *et al.* Determination of the diffusion coefficient of lithium ions in nano-Si. *Solid State Ionics* (2009) doi:10.1016/j.ssi.2008.12.015.
17. Prosini, P. P., Lisi, M., Zane, D. & Pasquali, M. Determination of the chemical diffusion coefficient of lithium in LiFePO4. *Solid State Ionics* (2002) doi:10.1016/S0167-

2738(02)00134-0.
18. Wen, C. J. & Huggins, R. A. Chemical diffusion in intermediate phases in the lithium-silicon system. *J. Solid State Chem.* (1981) doi:10.1016/0022-4596(81)90487-4.
19. Chen, Y. *et al.* Application of Galvanostatic Intermittent Titration Technique to Investigate Phase Transformation of LiFePO4 Nanoparticles. *Electrochim. Acta* (2017) doi:10.1016/j.electacta.2017.04.137.
20. Dees, D. W., Kawauchi, S., Abraham, D. P. & Prakash, J. Analysis of the Galvanostatic Intermittent Titration Technique (GITT) as applied to a lithium-ion porous electrode. *J. Power Sources* (2009) doi:10.1016/j.jpowsour.2008.09.045.
21. Chen, K., Pan, W. & Xue, D. Phase transformation of Ce3+-Doped MnO2 for pseudocapacitive electrode materials. *J. Phys. Chem. C* (2016) doi:10.1021/acs.jpcc.6b07708.
22. Takasaki, T. *et al.* Fiber-Type Ni(OH) 2 Electrode for Nickel-Metal Hydride Battery: Super High-Rate Charge/Discharge and Long Cycle-Life Performances . *J. Electrochem. Soc.* (2012) doi:10.1149/2.038211jes.
23. Funabiki, A. Stage Transformation of Lithium-Graphite Intercalation Compounds Caused by Electrochemical Lithium Intercalation. *J. Electrochem. Soc.* (1999) doi:10.1149/1.1391953.
24. Wang, C. & Hong, J. Ionic/electronic conducting characteristics of LiFePO4 cathode materials. *Electrochem. Solid-State Lett.* (2007) doi:10.1149/1.2409768.
25. Herle, P. S., Ellis, B., Coombs, N. & Nazar, L. F. Nano-network electronic conduction in iron and nickel olivine phosphates. *Nat. Mater.* (2004) doi:10.1038/nmat1063.
26. Williamson, G. A. *et al.* Temperature-Dependent Electrochemical Characteristics of Antimony Nanocrystal Alloying Electrodes for Na-Ion Batteries. *ACS Appl. Energy Mater.* (2019) doi:10.1021/acsaem.9b01216.
27. Darwiche, A., Bodenes, L., Madec, L., Monconduit, L. & Martinez, H. Impact of the salts and solvents on the SEI formation in Sb/Na batteries: An XPS analysis. *Electrochim. Acta* (2016) doi:10.1016/j.electacta.2016.03.089.
28. Li, Z. *et al.* Coupling in Situ TEM and Ex Situ Analysis to Understand Heterogeneous Sodiation of Antimony. *Nano Lett.* (2015) doi:10.1021/acs.nanolett.5b03373.
29. Caputo, R. An Insight into Sodiation of Antimony from First-Principles Crystal Structure Prediction. *J. Electron. Mater.* (2016) doi:10.1007/s11664-015-4260-0.
30. Allan, P. K. *et al.* Tracking Sodium-Antimonide Phase Transformations in Sodium-Ion Anodes: Insights from Operando Pair Distribution Function Analysis and Solid-State NMR Spectroscopy. *J. Am. Chem. Soc.* (2016) doi:10.1021/jacs.5b13273.
31. Cai, X. & Langtangen, H. P. Parallelizing PDE solvers using the Python programming language. *Lect. Notes Comput. Sci. Eng.* (2006) doi:10.1007/3-540-31619-1_9.
32. Mushtaq, A., Kvamsdal, T. & Olaussen, K. Python classes for numerical solution of PDE's. in *Lecture Notes in Engineering and Computer Science* (2015).
33. Gross, L., Cumming, B., Steube, K. & Weatherley, D. A python module for PDE-based numerical modelling. in *Lecture Notes in Computer Science (including subseries Lecture Notes in Artificial Intelligence and Lecture Notes in Bioinformatics)* (2007).
34. Lagadec, M. F., Zahn, R. & Wood, V. Characterization and performance evaluation of lithium-ion battery separators. *Nature Energy* (2019) doi:10.1038/s41560-018-0295-9.
35. Wang, H. Y. & Wang, F. M. Electrochemical investigation of an artificial solid electrolyte interface for improving the cycle-ability of lithium ion batteries using an atomic layer

deposition on a graphite electrode. *J. Power Sources* (2013) doi:10.1016/j.jpowsour.2013.01.134.
36. Lee, K. T., Jeong, S. & Cho, J. Roles of surface chemistry on safety and electrochemistry in lithium ion batteries. *Acc. Chem. Res.* (2013) doi:10.1021/ar200224h.
37. Cañas, N. A., Wolf, S., Wagner, N. & Friedrich, K. A. In-situ X-ray diffraction studies of lithium-sulfur batteries. *J. Power Sources* (2013) doi:10.1016/j.jpowsour.2012.10.092.
38. Holtstiege, F., Schmuch, R., Winter, M., Brunklaus, G. & Placke, T. New insights into pre-lithiation kinetics of graphite anodes via nuclear magnetic resonance spectroscopy. *J. Power Sources* (2018) doi:10.1016/j.jpowsour.2017.12.069.
39. Lombardo, L. *et al.* In-situ gelled electrolyte for lithium battery: Electrochemical and Raman characterization. *J. Power Sources* (2014) doi:10.1016/j.jpowsour.2013.06.087.
40. Itou, M. *et al.* Compton scattering imaging of a working battery using synchrotron high-energy X-rays. *J. Synchrotron Radiat.* (2015) doi:10.1107/S1600577514024321.
41. Torai, S., Nakagomi, M., Yoshitake, S., Yamaguchi, S. & Oyama, N. State-of-health estimation of LiFePO4/graphite batteries based on a model using differential capacity. *J. Power Sources* (2016) doi:10.1016/j.jpowsour.2015.11.070.
42. Hess, A. *et al.* Determination of state of charge-dependent asymmetric Butler-Volmer kinetics for LixCoO2 electrode using GITT measurements. *J. Power Sources* (2015) doi:10.1016/j.jpowsour.2015.07.080.
43. Verma, A. *et al.* Galvanostatic Intermittent Titration and Performance Based Analysis of LiNi 0.5 Co 0.2 Mn 0.3 O 2 Cathode . *J. Electrochem. Soc.* (2017) doi:10.1149/2.1701713jes.
44. Delacourt, C., Ati, M. & Tarascon, J. M. Measurement of Lithium Diffusion Coefficient in LiyFeSO4F. *J. Electrochem. Soc.* (2011) doi:10.1149/1.3581087.
45. Markevich, E., Levi, M. D. & Aurbach, D. Comparison between potentiostatic and galvanostatic intermittent titration techniques for determination of chemical diffusion coefficients in ion-insertion electrodes. *J. Electroanal. Chem.* (2005) doi:10.1016/j.jelechem.2005.03.030.
46. Shen, Z., Cao, L., Rahn, C. D. & Wang, C.-Y. Least Squares Galvanostatic Intermittent Titration Technique (LS-GITT) for Accurate Solid Phase Diffusivity Measurement. *J. Electrochem. Soc.* (2013) doi:10.1149/2.084310jes.
47. Morgan, D., Van der Ven, A. & Ceder, G. Li Conductivity in LixMPO4 (M = Mn, Fe, Co, Ni) Olivine Materials. *Electrochem. Solid-State Lett.* (2004) doi:10.1149/1.1633511.
48. Rui, X. H., Ding, N., Liu, J., Li, C. & Chen, C. H. Analysis of the chemical diffusion coefficient of lithium ions in Li3V2(PO4)3 cathode material. *Electrochim. Acta* (2010) doi:10.1016/j.electacta.2009.11.096.
49. Dibden, J. W., Meddings, N., Owen, J. R. & Garcia-Araez, N. Quantitative Galvanostatic Intermittent Titration Technique for the Analysis of a Model System with Applications in Lithium−Sulfur Batteries. *ChemElectroChem* (2018) doi:10.1002/celc.201701004.
50. Brevnov, D. A., Olson, T. S., López, G. P. & Atanassov, P. Electroless deposition of silver by galvanic displacement on aluminum alloyed with copper. *J. Phys. Chem. B* (2004) doi:10.1021/jp047096u.
51. Lu, D. L., Domen, K. & Tanaka, K. I. Electrodeposited Au-Fe, Au-Ni, and Au-Co alloy nanoparticles from aqueous electrolytes. *Langmuir* (2002) doi:10.1021/la010715v.
52. Pu, W., He, X., Ren, J., Wan, C. & Jiang, C. Electrodeposition of Sn-Cu alloy anodes for lithium batteries. *Electrochim. Acta* (2005) doi:10.1016/j.electacta.2005.01.041.

53. Ahmed, T. & Rack, H. J. Phase transformations during cooling in α + β titanium alloys. *Mater. Sci. Eng. A* (1998) doi:10.1016/s0921-5093(97)00802-2.
54. Porter, D. A., Easterling, K. E. & Sherif, M. Y. *Phase transformations in metals and alloys, third edition*. *Phase Transformations in Metals and Alloys, Third Edition* (2009).
55. Hillert, M. *Phase Equilibria, Phase Diagrams and Phase Transformations*. *Phase Equilibria, Phase Diagrams and Phase Transformations* (2007). doi:10.1017/cbo9780511812781.
56. Avrami, M. Kinetics of phase change. I: General theory. *J. Chem. Phys.* (1939) doi:10.1063/1.1750380.
57. Avrami, M. Kinetics of phase change. II Transformation-time relations for random distribution of nuclei. *J. Chem. Phys.* (1940) doi:10.1063/1.1750631.
58. Levi, M. D. & Aurbach, D. Frumkin intercalation isotherm - a tool for the description of lithium insertion into host materials: a review. *Electrochim. Acta* (1999) doi:10.1016/S0013-4686(99)00202-9.
59. Levi, M. D., Markevich, E. & Aurbach, D. The effect of slow interfacial kinetics on the chronoamperometric response of composite lithiated graphite electrodes and on the calculation of the chemical diffusion coefficient of Li Ions in graphite. *J. Phys. Chem. B* (2005) doi:10.1021/jp0441902.
60. Ling, Z. Lecture 4: Diffusion : Fick's second law. *Lecture* (2008).
61. Van Milligen, B. P., Bons, P. D., Carreras, B. A. & Śnchez, R. On the applicability of Fick's law to diffusion in inhomogeneous systems. *Eur. J. Phys.* (2005) doi:10.1088/0143-0807/26/5/023.
62. Coleman, S. P., Spearot, D. E. & Foiles, S. M. The effect of synthetic driving force on the atomic mechanisms associated with grain boundary motion below the interface roughening temperature. *Comput. Mater. Sci.* (2014) doi:10.1016/j.commatsci.2014.01.022.
63. Kim, H. J. & Cho, J. H. Driving force of phase transition in indium nanowires on Si(111). *Phys. Rev. Lett.* (2013) doi:10.1103/PhysRevLett.110.116801.
64. Yan, S., Pu, J., Chi, B. & Jian, L. Estimation of driving force for martensitic transformation in (Ni 52.5Mn23.5Ga24)100-xCox alloys. *J. Alloys Compd.* (2010) doi:10.1016/j.jallcom.2010.07.194.
65. Matson, D. M. Retained free energy as a driving force for phase transformation during rapid solidification of stainless steel alloys in microgravity. *npj Microgravity* (2018) doi:10.1038/s41526-018-0056-x.
66. Hillert, M., Odqvist, J. & Ågren, J. Interface conditions during diffusion-controlled phase transformations. *Scr. Mater.* (2004) doi:10.1016/j.scriptamat.2003.10.027.
67. Chandler, D. Interfaces and the driving force of hydrophobic assembly. *Nature* (2005) doi:10.1038/nature04162.
68. Trautt, Z. T., Upmanyu, M. & Karma, A. Interface mobility from interface random walk. *Science (80-.).* (2006) doi:10.1126/science.1131988.
69. Cahn, J. W. Theory of crystal growth and interface motion in crystalline materials. *Acta Metall.* (1960) doi:10.1016/0001-6160(60)90110-3.
70. Packham, D. E. Surface energy, surface topography and adhesion. *Int. J. Adhes. Adhes.* (2003) doi:10.1016/S0143-7496(03)00068-X.
71. Cahn, J. W. & Hilliard, J. E. Free energy of a nonuniform system. I. Interfacial free energy. *J. Chem. Phys.* (1958) doi:10.1063/1.1744102.
72. Santofimia, M. J., Zhao, L. & Sietsma, J. Model for the interaction between interface

migration and carbon diffusion during annealing of martensite-austenite microstructures in steels. *Scr. Mater.* (2008) doi:10.1016/j.scriptamat.2008.02.045.

73. Porter, D. A. & Easterling, K. E. *Phase Transformations in Metals and Alloys*. *Phase Transformations in Metals and Alloys* (1992). doi:10.1007/978-1-4899-3051-4.